NeuroImage: Clinical 26 (2020) 102185

Contents lists available at ScienceDirect

NeuroImage: Clinical

journal homepage: www.elsevier.com/locate/ynicl

Analyzing the co-localization of substantia nigra hyper-echogenicities and iron accumulation in Parkinson's disease: A multi-modal atlas study with transcranial ultrasound and MRI

Seyed-Ahmad Ahmadi[a,b,d], Kai Bötzel[a], Johannes Levin[a], Juliana Maiostre[a], Tassilo Klein[e], Wolfgang Wein[f], Verena Rozanski[g], Olaf Dietrich[c], Birgit Ertl-Wagner[c,h], Nassir Navab[d], Annika Plate[a,*]

[a] Department of Neurology, Ludwig-Maximilians University, Marchioninistraße 15, Munich 81377, Germany
[b] German Center for Vertigo and Balance Disorders (DSGZ), Ludwig-Maximilians University, Marchioninistraße 15, Munich 81377, Germany
[c] Department of Radiology, Ludwig-Maximilians University, Marchioninistr. 15, Munich 81377, Germany
[d] Chair for Computer Aided Medical Procedures (CAMP), Technical University of Munich, Boltzmannstr. 3, Garching 85748, Germany
[e] SAP ML Research, Berlin, Germany
[f] ImFusion GmbH, Agnes-Pockels-Bogen 1, München 80992, Germany
[g] Klinik Haag i. OB, Haag i. OB 83527, Germany
[h] The Hospital for Sick Children, 555 University Avenue, Toronto, Ontario M5G 1 × 8, Canada

ARTICLE INFO

Keywords:
Parkinson's disease
Transcranial sonography
Quantitative susceptibility mapping
Substantia nigra
Multi-modal registration

ABSTRACT

Background: Transcranial B-mode sonography (TCS) can detect hyperechogenic speckles in the area of the substantia nigra (SN) in Parkinson's disease (PD). These speckles correlate with iron accumulation in the SN tissue, but an exact volumetric localization in and around the SN is still unknown. Areas of increased iron content in brain tissue can be detected in vivo with magnetic resonance imaging, using quantitative susceptibility mapping (QSM).

Methods: In this work, we i) acquire, co-register and transform TCS and QSM imaging from a cohort of 23 PD patients and 27 healthy control subjects into a normalized atlas template space and ii) analyze and compare the 3D spatial distributions of iron accumulation in the midbrain, as detected by a signal increase (TCS+ and QSM+) in both modalities.

Results: We achieved sufficiently accurate intra-modal target registration errors (TRE < 1 mm) for all MRI volumes and multi-modal TCS-MRI co-localization (TRE < 4 mm) for 66.7% of TCS scans. In the caudal part of the midbrain, enlarged TCS+ and QSM+ areas were located within the SN pars compacta in PD patients in comparison to healthy controls. More cranially, overlapping TCS+ and QSM+ areas in PD subjects were found in the area of the ventral tegmental area (VTA).

Conclusion: Our findings are concordant with several QSM-based studies on iron-related alterations in the area SN pars compacta. They substantiate that TCS+ is an indicator of iron accumulation in Parkinson's disease within and in the vicinity of the SN. Furthermore, they are in favor of an involvement of the VTA and thereby the mesolimbic system in Parkinson's disease.

1. Introduction

Ferric iron (Fe^{3+}) is suspected to accelerate the pathological aggregation of α-synuclein, which is the core pathophysiological process in Parkinson's disease (PD) (Levin et al., 2011). Iron ions are increased in the midbrain and substantia nigra (SN) tissues of PD patients, whether this is causative for or a consequence of the disease is unknown (Sofic et al., 1988; Dexter et al., 1991; Gerlach et al., 1994). A reference technique for precise, MRI-based in-vivo localization of iron in the brain is quantitative susceptibility mapping (QSM), which was shown to measure increased iron accumulation (QSM+) in and around the SN, in particular in the pars compacta (Barbosa et al., 2015; Murakami et al., 2015; Du et al., 2016; An et al., Jan. 2018; Langkammer et al., 2012; Bergsland et al., 2019).

* Corresponding author.
E-mail address: Annika.plate@med.uni-muenchen.de (A. Plate).

https://doi.org/10.1016/j.nicl.2020.102185
Received 1 September 2019; Received in revised form 12 January 2020; Accepted 14 January 2020
Available online 01 February 2020

Transcranial sonography (TCS) is a non-invasive imaging modality for assessing deep brain regions through the pre-auricular bone window. In idiopathic PD, TCS is an established tool for early detection (Berg et al., Jul. 2011; Berg et al., 2013) and non-invasive quantification of pathophysiological changes in the SN. While the SN appears as bright, visible speckle (TCS+) in the midbrain parenchyma in both healthy controls (HC) and patients with PD, an increased area ("hyperechogenicity") of the SN can serve as a biomarker for detection of PD (Becker et al., 1995; Walter et al., 2007; Van De Loo et al., 2010; Berg, 2006). Recently, the results of multiple studies were analyzed in two meta-analyses, which concluded a pooled sensitivity of 83% and specificity of 87% for distinguishing PD patients from HC (Li et al., 2016), and a pooled sensitivity of 75% and specificity of 70% for discrimination of atypical parkinsonism from PD (Shafieesabet et al., Sep. 2017). In 2013, the European guidelines for diagnosis of PD were amended with a level A recommendation for TCS examination (Berardelli et al., 2013).

The physical formation process of TCS+ speckles is associated with increased iron accumulation as well. This was shown in postmortem TCS of the midbrain parenchyma and histochemical analysis of SN tissue in animal (Berg et al., 1999) and human postmortem studies (Berg et al., 2002), where a significantly positive correlation of TCS+ area with iron accumulation in the SN was found. However, a detailed analysis of the 3D spatial distribution of TCS+ has not been described in literature yet. Here, we investigate for the first time, where TCS+ speckle patterns actually occur with respect to the SN and elsewhere in the midbrain, whether these locations correspond to known locations of PD-related nigral injury and whether there is a difference in the spatial distribution of TCS+ in HC and PD.

The common clinical practice of 2D TCS acquisition (Berardelli et al., 2013) yields diagnostically reliable quantifications of 2D SN area, but precludes volumetric analyses of the 3D spatial distribution of the TCS+ speckle. Previously, we have introduced 3D TCS with the goal of increasing the objectivity of the TCS diagnostic examination (Plate et al., 2012), along with computer-aided methods for segmentation and analysis of midbrain parenchyma and TCS+ regions (Ahmadi et al., 2011; Pauly et al., 2012; Kroll et al., 2016; Milletari et al., 2017). In this study, we aimed to co-localize 3D-TCS+ and QSM+ in a group-analysis, to further our understanding of the TCS imaging technique and of the occurrence of pathophysiological findings in PD.

2. Materials and methods

Key elements of the study design are summarized in Fig. 1.

2.1. Study population

This prospective study was approved by the local ethics committee. All study participants ($N = 50$; HC: $N = 27$; PD: $N = 23$) gave their written informed consent. PD patients were recruited and examined during a period of 6 months from the outpatient clinic of the department of neurology. An age of 18 years or above and no history of brain surgery served as the general inclusion criteria. Patients were diagnosed according to the criteria of the United Kingdom Parkinson's Disease Society Brain Bank for idiopathic Parkinson's disease (Hughes et al., 1992). Age-matched healthy controls were partners and/or friends of PD patients. Additional inclusion criteria for HC subjects were a negative medical history for neurological diseases and a clinical neurological examination without abnormal findings. A further inclusion criterion for the whole cohort was a sufficient insonification for TCS examination through the pre-auricular bone window. Further obtained information included age, gender, Hoehn&Yahr stage (H&Y), Unified Parkinson's Disease Rating Scale (UPDRS) part III, Montreal Cognitive Assessment (MoCA) and disease duration. The PD group was heterogeneous regarding dominant side (10 L, 10 R, 3 None), and motor subtype (9 akinetic-rigid, 11 tremor-dominant, 3 mix-type). Table 1 provides further details on the two cohorts that were included in the QSM-MRI and TCS atlas.

2.2. MRI and QSM acquisition

MRI acquisition was performed with a 3 Tesla whole-body MRI system, featuring a 32-channel head-coil (Magnetom Verio, Siemens Healthineers, Erlangen, Germany). A 3D multi-echo spoiled gradient-echo sequence was used for recording QSM and R_2* data (Schweser et al., 2011) (TR: 41 ms, TE:10, 20, 30 ms, flip angle: 20°, isotropic resolution of $1 \times 1 \times 1$ mm^3 (interpolated based on phase and slice resolution of 80%), no parallel imaging, matrix size (readout × phase × slice direction): $256 \times 192 \times 144$, receiver bandwidth: 130 Hz/pixel, acquired in axial orientation, total acquisition time 9:38 min). In the following, image data of this acquisition are referred to as T2*w(10 ms), T2*w(20 ms), and T2*w(30 ms).

As anatomical reference, a T1-weighted (T1w) 3D Magnetization Prepared RApid Gradient Echo (MPRAGE) sequence was acquired (TR: 1800 ms, TE: 3 ms, TE: 900 ms, flip angle: 9°, isotropic resolution of $1 \times 1 \times 1$ mm^3, parallel imaging acceleration factor: 2, matrix size (readout × phase × slice direction): $256 \times 240 \times 160$, receiver bandwidth: 230 Hz/pixel, acquired in sagittal orientation, total acquisition time 3:40 min).

The multi-echo gradient-echo data were post-processed by brain extraction with FSL bet (Smith, 2002), followed by an estimation of phase evolution over all three echo times (Bernstein et al., 1994). The original phase information was replaced by phases calculated from the weighted sum of complex quotients to remove open-fringe-line artifacts caused by imperfect multi-channel data combination. Further processing was based only on these relative phase data at an echo time of 10 ms. Susceptibility maps were calculated from the wrapped phase data using a fast QSM technique based on a total-generalized-variation (TGV) approach (Langkammer et al., 2015) with the recommended regularization parameter $\alpha_1 = 0.0015$.

2.3. 3D-TCS acquisition, TCS+ segmentation and registration to MRI

Transcranial ultrasound was acquired with a freehand 3D setup for all subjects in our cohort (cf. Table 1) (Plate et al., 2012). An optical tracking camera (NDI Polaris Spectra; Northern Digital Inc, Waterloo, ON, Canada) recorded the 3D pose of the ultrasound probe and the patient head motion during B-mode sonography (Sonix MDP, Ultrasonix, BK Medical, MA, USA). Ultrasound images and temporally synchronized tracking data were recorded and reconstructed offline into a 3D volume at an isotropic voxel resolution of $0.5 \times 0.5 \times 0.5$ mm^3 using a backward compounding scheme (Wein et al., 2006) (Gaussian distance kernel, s.d. = 1 voxel). A part of the head surface was probed with a tracked pointer (i.e. stylus) for initial surface registration to MRI.

The scanning procedure was performed by positioning the transducer on the pre-auricular bone window and setting the plane parallel to the orbito-mental line and turning the frontal part of the transducer a little more downward (semi-axial). From a midbrain cross-section position, the image plane was tilted downwards in caudal direction until the brainstem was visible. This is where 3D acquisition was started, from there going upwards until the third ventricle and beyond. It is important to note that in the 3D method, an exact positioning or orientation of the transducer is not as vitally important as in the 2D TCS method. The 3D reconstruction corrects for the 3D transducer pose (i.e. translation and rotation), resulting in an isotropic voxel grid, regardless of the examiner-led trajectory.

TCS volume data was acquired separately on each left and right side, by with two to five 3D-TCS sweeps per side. Two raters (authors AP and AA) jointly selected one 3D-TCS sweep with maximum clarity and contrast for each side, before proceeding with quantitative analyses. Both raters proceeded by manually segmenting each TCS scan in a

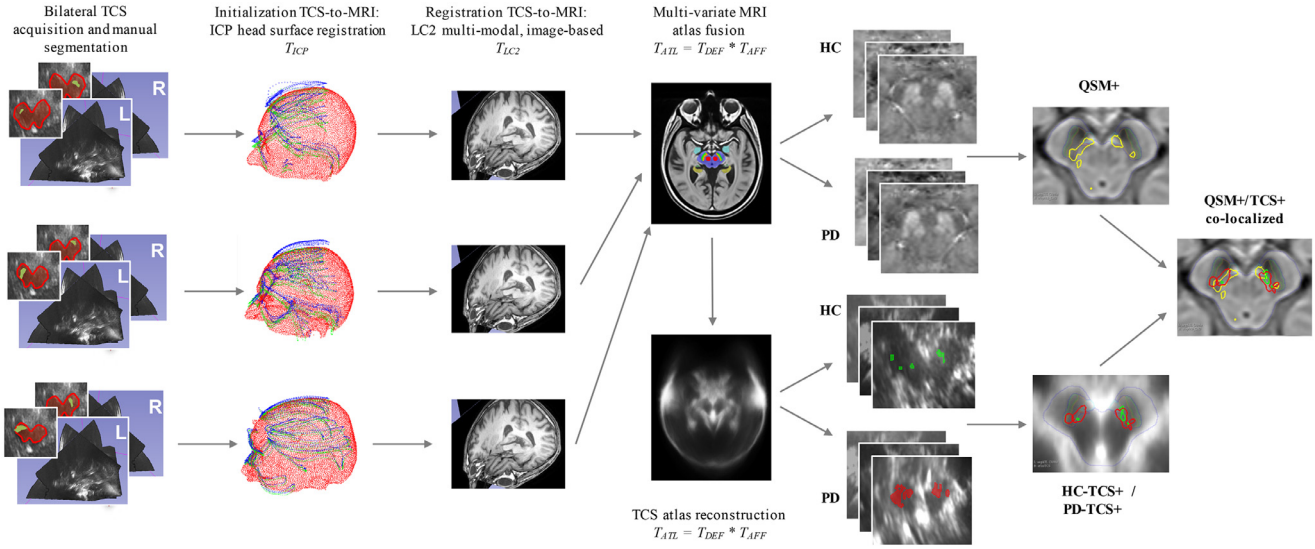

Fig. 1. Graphical abstract for multi-modal TCS-MRI atlas creation: 2D TCS images are acquired and 3D TCS volumes of the midbrain region are reconstructed. TCS+ voxels ipsilateral to the transducer are manually segmented. Each 3D TCS volume is registered to the same participant's cranial MRI scan via initial head surface alignment and subsequent fine-tuning using a multi-modal ultrasound-MRI intensity-based registration algorithm. An average brain template is created from MRI using a multi-variate optimal template building approach. The resulting transformations are used to deform TCS images and TCS+ segmentations into template space. Here, group analysis is performed on QSM-MR image volumes using voxel-wise statistical testing to localize QSM+ voxels with statistically significant difference between HC and PD (yellow contours). Group-wise TCS+ is localized separately for HC (green contours) and PD (red contours) by voxel-wise thresholding at 50% of the group size (i.e. majority voting). Co-localization of QSM+ and TCS+ is analyzed qualitatively and quantitatively, in particular with respect to the SN area (dark green contour: SN pars reticulate, dark brown contour: SN pars compacta).

Table 1
Cohort details: demographic data for HC and PD subgroups, as well as details on disease status in the PD sub-group. The full cohort is included in QSM-MRI analysis. The TCS atlas considers a sub-cohort, which results from only including TCS scans with accurate TCS-MRI registration accuracy. (M: male; F: female; L: left; R: right).

		Full cohort in QSM-MRI atlas				Sub-cohort in TCS atlas			
		mean	s.d.	min	max	mean	s.d.	min	max
Healthy controls (N = 27)	Total group size	N = 27				N = 22			
	Gender	13 F / 14 M				12 F / 10 M			
	Number of 3D TCS volumes	25 L / 27 R				22 L / 17 R			
	Age [years]	65,7	6,5	47	78	65,6	6,5	47	78
PD patients (N = 23)	Total group size	N = 23				N = 12			
	Gender	10 F / 13 M				6 F / 6 M			
	Number of 3D TCS volumes	22 L / 22 R				12 L / 12 R			
	Age [years]	68,8	8,7	41	82	66,3	9,4	41	79
	PD Hoehn&Yahr	1,85	0,65	1	3	1,83	0,72	1	3
	PD UPDRS	30,3	14,2	10	66	27,9	13,1	10	57
	PD MoCA	25,4	3,8	15	30	25,4	3,2	18	30
	PD Duration [years]	8,5	4,4	2	20	8,1	3,8	2,5	15

slice-by-slice fashion (Yushkevich et al., 2006) to localize TCS+ ipsilateral to the transducer. Following Plate et al. (Plate et al., 2012), TCS + segmentation started at 1.5 mm (3 slices) caudal to the lowest visibility of the third ventricle, and continued until the midbrain or TCS+ boundaries became indiscernible to the background. During manual annotation, raters were blinded to the participant's identity, meta-information (age, gender), medical information, or structure from MRI.

Finally, TCS images were automatically registered to MRI in a multi-modal, intra-subject manner, to spatially align TCS intensities with the subject's MRI scan. First, an initial head-surface registration was automatically computed with the Iterative Closest Points (ICP) algorithm (Ahmadi et al., 2015). Second, the initial registration was refined through intensity-based registration based on LC2, a state-of-the-art multi-modal similarity metric for ultrasound-MRI alignment (Wein et al., 2013; Fuerst et al., 2014). The matching was performed in a slice-to-volume approach, iteratively optimizing the transformation parameters of the original tracked freehand ultrasound slices to maximally resemble matching MRI slices (Fuerst et al., 2014). To compensate for geometric distortion of TCS through the bone window, the transformation model allowed simple scaling of TCS images along the y-axis, which is caused by sound speed differences through bone vs. brain tissue.

2.4. Multi-variate MRI/TCS atlas building and iron+ localization

After TCS-to-MRI registration, image volumes from all study participants were spatially normalized into a common template space, which was created from multiple MRI contrasts. The MR image contrasts used for each subject were T1w, and T2*w(10 ms) and T2*w(30 ms). A multi-variate template MRI was computed using an algorithm for unbiased, multi-variate optimization of brain morphology and appearance, provided in the ANTs normalization toolkit (Avants et al., 2010). Further parameters were set to: transformation model: greedy SyN; similarity metric: local cross-correlation; multi-resolution registration: four levels (downsampling factors: 8,4,2,1; smoothing sigmas: 3,2,1,0 mm; maximum iterations: 100,70,50,10).

In template space, two clinical expert raters (authors AP and VR) manually segmented the multi-variate MRI image data in a slice-by-

slice fashion (Yushkevich et al., 2006). Segmented regions included the midbrain (MB), substantia nigra pars compacta (SNc), substantia nigra pars reticulata (SNr), red nucleus (RN), and two sub-regions of VTA, the rostral ventral tegmental area (rVTA) and parabrachial pigmented nucleus (PBP). Region segmentation of SNc, SNr, RN, and MB were based on multi-variate visibility in MRI. The VTA regions (rVTA and PBP) were segmented according to rules defined in Murty et al. (Murty et al., 2014), and cytoarchitecture outlined in Büttner-Enever et al. (Büttner-Ennever and Horn, 2014). Segmentations of both raters were fused with voxel-wise majority voting after label-wise Gaussian smoothing (s.d. = 1 mm).

The corresponding TCS atlas was built by applying the transformations computed during MRI template normalization. TCS volumes with insufficient overlap with MRI (see next section) were discarded, i.e. only a sub-cohort is considered in the TCS template (see Table 1). In template space, TCS scans were winsorized [5% − 95%], normalized ([0,1] intensity range) and an average TCS template was computed, yielding probabilistic maps for hyperechogenicities of the SN.

2.5. Validation of registrations

Registration quality was validated through accuracy and precision of the target registration error (TRE) (Jannin et al., 2002), computed as the mean Euclidean distance between a set of manually selected landmarks in volume pairs (author AA). These pairs were selected to evaluate the full registration pipeline in two steps, first for TCS-to-MRI registration, and second for MRI-to-atlas registration. To estimate the axial registration accuracy, we use the pineal gland, which reliably appears as a bright hyperechogenic ellipsoid of roughly 5 mm diameter in TCS due to its naturally occurring calcifications. In lateral direction, we used the midbrain and third ventricle to estimate anatomic surface registration error in the horizontal image plane. A set of 10 landmark points distributed along the boundary of the midbrain, and two points on the lateral walls of the third ventricle were used to evaluate lateral and anterior-posterior registration fidelity.

The same protocol of landmark TRE estimation was performed in MRI volume pairs and the MRI atlas. In-plane registration accuracy of the midbrain and third ventricle were estimated by 2D displacement of the same set of landmarks as in TCS. Given better structural visibility in MRI, we tagged four further 3D landmarks in MRI: red nucleus centroid left/right, anterior commissure (AC) and posterior commissure (PC).

2.6. Statistical analysis and localization of TCS+ and QSM+

In QSM MRI, we performed a group analysis to localize voxel regions with increased susceptibility (iron accumulation) in the PD cohort. We computed non-parametric statistical tests (unpaired, one-sided Wilcoxon test) for all voxels inside the midbrain, followed by multiple comparison correction with the false discovery rate (FDR) algorithm (Jenkinson et al., 2012), the q-rate set to an alpha-level of $p < 0.05$, and masked with the midbrain atlas segmentation. All manual segmentations of TCS+ were transformed into template space and averaged in order to create probabilistic TCS+ labelmaps separately for HC and PD. To identify group-wise TCS+ regions, we thresholded the probabilistic TCS+ labelmaps at a level of 0.5 (i.e. majority consensus voting), which increases robustness to noisy segmentations and inter-subject differences in TCS+ localizations (Xu et al., 2017; Schaefer et al., 2016) and thus provides an unbiased and conservative estimate of the segmentation consensus. Group comparisons and correlation tests between clinical parameters and values of TCS+/QSM+ distributions were performed using two-sided parametric (*t*-test, Pearson's correlation) and non-parametric (Mann Whitney U test, Spearman's correlation) procedures (significance levels $p < 0.05$). All tests and correlation calculations were preceded by a Shapiro-Wilk test of normality (non-parametric results are reported for significance levels below $p < 0.05$). Voxel regions with QSM+ and TCS+ for HC and PD were then triangulated with surface meshes for visualization using 3D Slicer (Kikinis et al., 2014).

3. Results

3.1. Cohort details

Details for the healthy controls and PD patients in the full cohort are given in Table 1. There is no statistically significant difference between the number of male and female members in the HC vs PD groups, neither in the full cohort (Fishers exact test, $p = 0.964$), nor in the sub-cohort selected for the TCS atlas (Fishers exact test, $p = 0.731$). There is also no statistically significant difference in the age of both groups, neither in the full cohort (independent *t*-test, $p = 0.184$), nor in the sub-cohort selected for the TCS atlas (independent *t*-test, $p = 0.504$). The TCS atlas contains a sub-cohort of those subjects for whom the TCS scans could be registered with MRI with sufficient accuracy (see next section). Details for the sub-cohort are given in Table 1 as well.

3.2. Registration accuracy and selection of final selected cohorts in the atlas

The registration accuracy between 3D and 2D surface landmarks tagged in the atlas and each individual's MRI is denoted as “ATL-MRI” in Table 2. 3D landmarks between atlas and MRI were registered with a mean TRE of 0.67 mm (s.d. = 0.42 mm). We also evaluated intra-rater variability for multiple MRI landmark annotations (two times, rater: AA), resulting in a mean TRE of 0.45 mm ($\sigma = 0.37$ mm). In summary, ATL-MRI registration is accurate, with a mean TRE smaller than the MRI voxel size (1.0 mm), and comparable to intra-rater variability.

Concerning landmark registration between TCS and MRI, the pineal gland is localized in 3D TCS with a mean TRE of 3.04 mm (s.d. 1.78 mm). 2D surface distance points at height of the third ventricle and midbrain are registered with 2.07 mm mean TRE (s.d. 1.62 mm).

We defined quality thresholds for inclusion of TCS scans into the atlas based on two requirements: i) a median surface distance below 4 mm and ii) a 3D localization error of the pineal gland below 4 mm. Of the 96 scans recorded and considered in this study, 64 (66.7%) scans from 36 subjects matched this requirement and were included in the final TCS template. This results in a sub-cohort for the TCS template, compared to the full cohort included in the MRI template space, with demographics detailed in Table 1.

It is known that old age and female sex are related to bone windows with higher sound attenuation, refraction and phase aberration properties (Brunser et al., 2012; Ivancevich et al., 2006), which can lead to TCS images with lower overall quality. This, however, did not have a significant influence on average registration accuracy. The registration error was lower in female (median: 2.09) versus male participants (median: 2.47), but this difference was not significant (Mann-Whitney U, $p = 0.077$). Further, subject age and registration error are negligibly and not significantly correlated (Spearman's rank correlation, $r = 0.207$, $p = 0.052$).

Table 2
Statistics of landmark registration accuracy (TRE): on 96 TCS scans after intra-subject registration to MRI. (CP: corpus pineale, RN: red nucleus; AC/PC: anterior/posterior commissure; MB: midbrain; TV: third ventricle).

Registration accuracy in [mm]	MRI intra-rater	ATL-MRI	TCS-MRI
3D landmarks	(CP, RN, AC, PC)	(CP, RN, AC, PC)	(CP)
mean	0.452	0.671	3.037
s.d.	0.372	0.421	1.778
max	3.370	3.173	8.529
2D surface distance	(MB, TV)	(MB, TV)	(MB, TV)
mean	0.412	0.590	2.066
s.d.	0.323	0.356	1.615
max	4.018	3.402	11.892

Table 3
Localization of iron accumulation: Overlap (absolute in [mm^3] and relative in [%]) of TCS+ HC, TCS+ PD and QSM+ with different anatomic regions (left) and with each other (right). (SNc: substantia nigra pars compacta; SNr: substantia nigra pars reticulata; rVTA: rostral part of ventral tegmental area; PBP: parabrachial pigmented nucleus; RN: red nucleus; MB: midbrain; PD: Parkinson's disease patients; HC: healthy controls; TCS+: volume of transcranial sonography hyperechogenicity; QSM+: volume of voxels with significantly increased signal of PD vs. HC in quantitative susceptibility mapping MRI).

Overlap [mm^3]	SNc	SNr	rVTA	PBP	RN	MB	TCS+ PD	TCS+ HC	QSM+
TCS+ PD	112.7	31.3	14.2	8.8	19.1	101.1	333.7	54.8	68.5
TCS+ HC	30.8	2.9	4.0	5.4	13.3	26.0	54.8	109.9	6.4
QSM+	54.2	9.0	23.5	4.8	14.9	42.5	68.5	6.4	148.9
Overlap [%]									
TCS+ PD	39.3	10.9	4.9	3.1	6.6	35.2	100.0	16.4	20.5
TCS+ HC	37.4	3.5	4.9	6.5	16.2	31.6	49.8	100.0	5.9
QSM+	36.4	6.0	15.8	3.2	10.0	28.5	46.0	4.3	100.0

3.3. Localization of QSM+

QSM+ voxels, which represent statistically significant signal difference between HC and PD (full cohort, Table 1), are shown as bright yellow outlines in the midbrain in Fig. 2 (top panel). Qualitatively, the location of QSM+ voxels has a high overlap in the caudal regions of the hypo-intense bands belonging to the SN. In cranial direction, QSM+ regions move increasingly toward the medial direction. This is particularly noticeable in slices above 9 mm caudal of the AC-PC line, in which very few statistically significantly different voxels are located in hypo-intense SN regions, and more in the narrow region between SN and RN. According to cyto-architectural descriptions of the brainstem, this region between SN and RN can be attributed to the VTA area, more precisely PBP and rVTA (Büttner-Ennever and Horn, 2014). Quantitatively, the distribution of QSM+ total volume across different anatomic regions is detailed in Table 3. The total volume of QSM+ in template space is 148.9 mm^3, mainly distributed across midbrain parenchyma (42.5 mm^3 or 28.5% of QSM+ total volume), SNc (54.2 mm^3 or 36.4%) and rVTA (23.5 mm^3 or 15.8%). There is a slight laterality of QSM+ visible in Fig. 2, and 3 with more QSM+ present in the right side of the midbrain. This phenomenon cannot be attributed to the PD dominant side. First, there were exactly 10 left- and 10 right-dominant subjects in the cohort (3 mixed, see Table 1). Second, a higher iron amount in the right midbrain cannot be explained by higher UPDRS in the left-dominant group (t-test, $p = 0.987$). Neither can it be explained by a longer duration in the left-dominant group (t-test, $p = 0.581$). Apart from considering laterality, average QSM intensities are positively and significantly correlated (Pearson's correlation, $p < 0.05$) with UPDRS scores in regions SNr ($r = 0.415$), SNc ($r = 0.442$) and NPP ($r = 0.379$), while correlations in regions RN, MB and VTA are not significant. We also investigated a connection between iron contents and cognitive performance measured by MoCA scores (see Table 1). MoCA scores did not correlate significantly with iron contents in any of the investigated anatomic regions.

3.4. Localization of TCS+

In a related study of the TCS data in our cohort (Plate et al., 2019), we showed that segmented TCS+ volumes are statistically significantly different between PD and HC subjects (two-tailed Wilcoxon rank-sum test, $p < 0.001$), and that measured volumes can discriminate PD and HC with a 84.6% sensitivity and 88.9% specificity. Compared to that study, we focus here on the localization of TCS+. To this end, quantitative volume measurements of TCS+ for HC and PD (TCS sub-cohort, Table 1), both absolute in mm^3 and relative in%, are given in Table 3, along with measurements of overlap with anatomical regions in the midbrain.

A notable and expected visual result is that the TCS+ region appears larger in the PD patient sub-cohort than in the HC group (Fig. 2, middle panel). In terms of volume, the PD group, with a total volume of 333.7 mm^3 of TCS+, has a three times higher volume of hyperechogenicities than the HC group with 109.9mm^3. Regarding group overlap, it is notable that roughly half of TCS+ volume in HC (54.8 mm^3 or 49.8%) is co-located with TCS+ in PD.

Similar to QSM+, TCS+ regions have a high overlap with the SNc in the caudal area of the midbrain. More cranially, TCS+ is also located more medially of the SN, and to a large degree in the regions between RN and SN, i.e. PBP and rVTA. In numbers, TCS+ is largely localized in SNc for both the PD (112.7 mm^3 or 39.3%) and HC (30.8 mm^3 or 37.4%) groups.

Compared to QSM+, UPDRS and volume of hyperechogenicities show no significant correlation (Spearman rank correlation, $r = 0.090$, $p = 0.662$), which is in line with our previous study (Plate et al., 2019), and findings by other groups in literature (Walter et al., 2007; Michaeli et al., 2007; Jesus-Ribeiro et al., 2016; Lobsien et al., 2012).

3.5. Co-Localization of QSM+ and TCS+

Finally, the co-localization analysis of QSM+ and TCS+ is visualized in Fig. 3 and in Fig. 2 (bottom image panel set), which depicts all three regions at once, i.e. QSM+ (yellow outlines) and TCS+ in HC (green) and PD (red), overlaid on top of the T2*w(30 ms) MRI template, including atlas structures in the background. TCS+ and QSM+ have a large overlap, in particular between TCS+ of PD patients. In both modalities, a similar shift of TCS+ and QSM+ voxels towards the medial direction can be observed when moving the axial slice in cranial direction. Quantitatively, the overlap of TCS+ in HC and PD is given in detail in Table 3. One notable result is that almost half of QSM+ (46.0%) is overlapping with TCS+ regions of PD patients, while only 4.3% of the QSM+ region overlaps with hyperechogenic regions of HC subjects.

4. Discussion

In our study, we have analyzed the volumetric distribution of iron accumulation in a normalized template space, as detected by QSM+ and TCS+ in our cohort. Given our registration approach, two thirds (66.7%) of TCS scans could be transformed into the QSM-MRI template with sufficient landmark localization accuracy. In template space, iron accumulation in the midbrain was co-localized by both TCS+ and QSM+ along the entire midbrain's axial extent, and main sites of overlap could be localized in the areas of SNc and VTA.

4.1. Image registration approach and accuracy

We validated the accuracy of several registration methods, which lie at the basis of this study. The MRI template creation algorithm that we used constructs a geodesically optimal shape and appearance template (Avants et al., 2010), based on symmetric normalization (SyN), which is consistently reported as top-performing in various medical image registration challenges (Klein et al., 2009; Menze et al., 2015; Murphy et al., 2011). In our study, average MRI-to-atlas registration

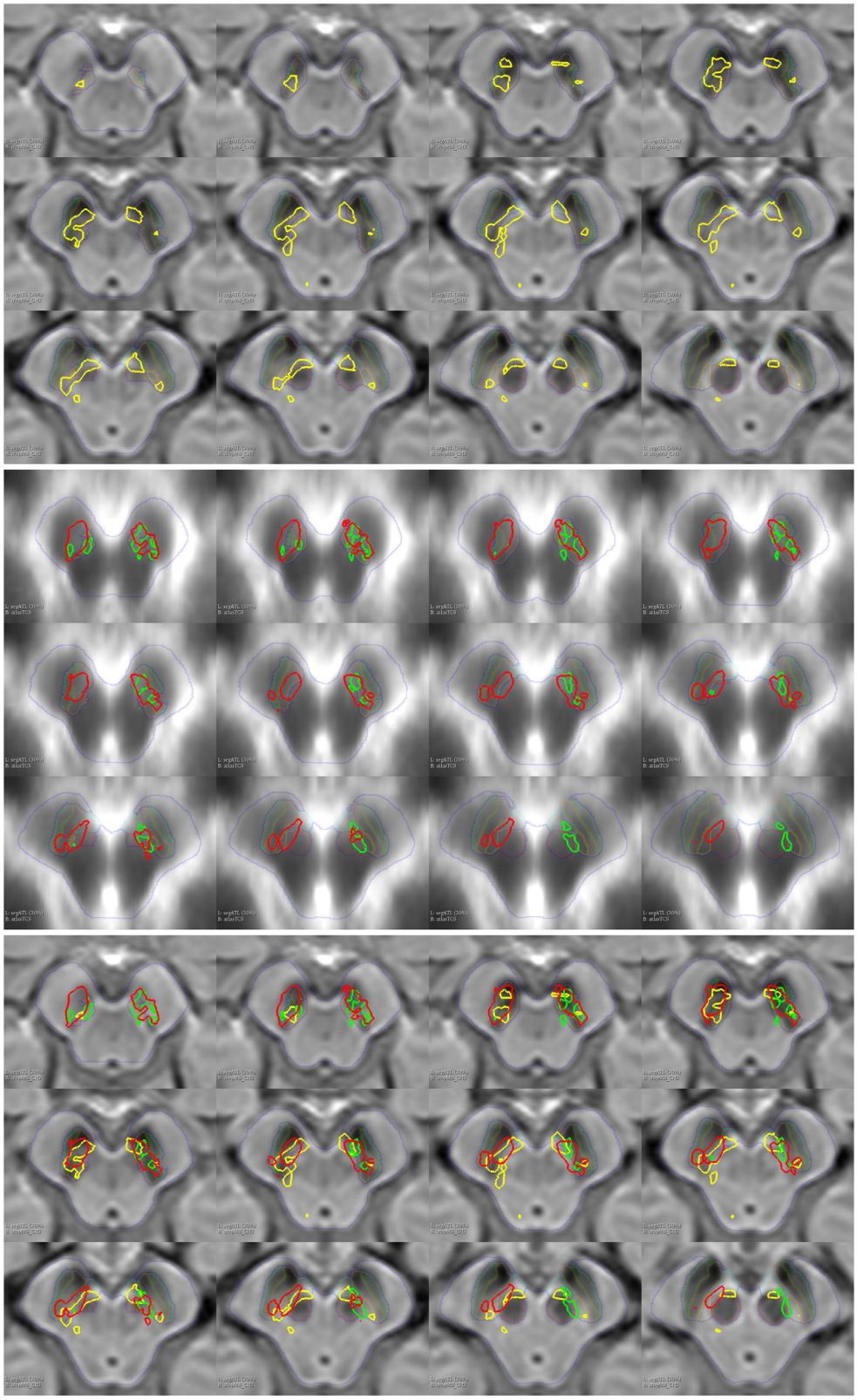

Fig. 2. Localization of QSM+ and TCS+. Smaller image panels show axial slices through the T2*w(30 ms) template MRI from −12 mm (top-left) to −6.5 mm (bottom-right), caudal of the AC-PC line, and in 0.5 mm slice distances. Expert-segmented atlas structures are delineated with faint colors (blue: MB, green: SNr, brown: SNc, cyan: VTA, yellow: PBP, red: RN). Upper panel: Bright yellow outlines indicate QSM+ regions, i.e. voxels with significantly higher iron accumulation in PD patients compared to a group of normal controls (yellow outlines). Middle panel: TCS+ HC delineated with bright green color, and TCS+ PD with bright red. Bottom panel: Co-localization of QSM+ and TCS+ in template space. Again, yellow indicates significant QSM+ regions, green and red represent TCS+ regions of HC and PD groups, respectively.

errors were measured on the order of 0.7 mm (cf. Table 2), i.e. only slightly larger than the intra-rater variability for tagging of the evaluated landmarks (0.5 mm), and below voxel spacing (1.0 mm). We therefore consider MRI-to-atlas registration errors as largely negligible in our study.

Concerning TCS-MRI registration, we are aware of two works that have previously demonstrated the feasibility of this task. Both works investigated TCS-based electrode localization in the context of deep-brain-stimulation neurosurgery (DBS). Walter et al. (Walter et al., 2016) investigated post-operative TCS imaging and visually concluded that TCS and MRI can be co-localized with a high degree of overlap. Their registration approach comprised two steps as well, first an

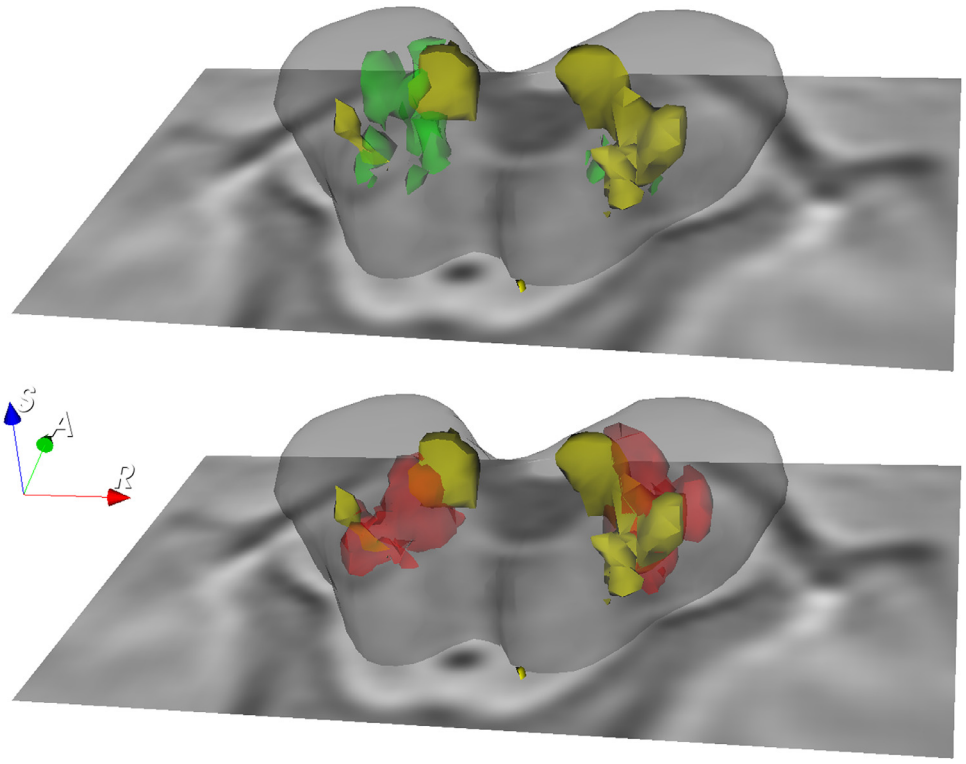

Fig. 3. Localization of QSM+ and TCS+ in 3D. As in Fig. 2, regions QSM+ (yellow), TCS + HC (green, top figure), and TCS+ PD (red, bottom figure) are visualized in template space, along with a caudal slice of the midbrain region from the T2*w(30 ms) template. A surface model of the midbrain region (extracted from the TCS atlas template) is shown for reference. The 3D coordinate vectors indicate the right (R), anterior (A) and superior (S) direction.

automated registration under aid of the navigation/tracking system, followed by manual-visual refinement of the MRI-TCS super-imposition. In our own previous work (Ahmadi et al., 2015), post-operative landmark-based registration resulted in a mean accuracy of 3.2 mm, and electrode tip localization was possible with a mean accuracy of 4.8 mm. Compared to these landmark- and manual interaction-based approaches, we have demonstrated in our work that in 66.7% of cases, intensity-based TCS-MRI registration was feasible and accurate. In the domain of multi-modal ultrasound-MRI registration, the LC2 similarity metric is currently state-of-the-art, having recently out-performed a range of competitive methods in a publicly held challenge on intra-operative brain shift compensation (Wein, 2018). The residual landmark registration in our study resulted in a mean accuracy of 3.0 mm, slightly lower than in our previous study (Ahmadi et al., 2015). Notably, this result is achieved fully automatically and without a lengthy and potentially biased selection of landmarks by experts. The fact that roughly one third of 3D TCS scans could not be accurately registered still poses a current limitation, which will be discussed further below.

A final discussion point on image registration accuracy is whether a residual 3 mm registration uncertainty between TCS and MRI in individuals had an impact on the localization of TCS+ hyper-echogenicities in template space, especially whether this affected the conclusions regarding the co-localization with QSM+. To answer this question, we performed an auxiliary experiment to investigate the effects of registration of all individuals' data into template space, in particular whether the super-imposition led to a potential down-averaging of localization errors. Considering eight of the landmarks on the midbrain boundary (distributed around the locations of the left and right SN), along with the 3D location of the pineal gland, we measured the intra-individual landmark distances between TCS and MRI, and compared it to the distance between the down-averaged TCS landmark locations (after deformation into template space and 3D coordinate averaging) and the MRI-atlas landmark locations. On average, the down-averaging improved the landmark localization errors from 2.4 mm to 1.2 mm. Notably, the 3D localization error of the pineal gland improved from 3.2 mm to 1.4 mm. This indicates that down-averaging and super-imposition of TCS/TCS+ results in template space leads to a reduction of localization errors. The resulting localization error is roughly on the order of the MRI voxel resolution (1 mm), and roughly on the order of the native imaging resolution (1.05 mm) of modern TCS imaging systems (Walter et al., 2008), i.e. within the technical feasibility of single-individual TCS+ localization. We are therefore confident that the TCS +/QSM+ co-localization results in template space, as well as the conclusions made thereof, are accurate and reliable.

4.2. Neurophysiological implications

Earlier studies have revealed iron being involved in neurodegenerative processes seen in PD (Gerlach et al., 1994; Dexter et al., 1987; Youdim et al., 1993). Iron accumulation within the dopaminergic neurons in the SN, especially the pars compacta, are considered to be an epiphenomenon or even an underlying factor of PD and its symptoms (Ayton and Lei, 2014; Lotfipour et al., 2012). In TCS, hyperechogenicities and their higher iron content have been measured spectroscopically in animal (Berg et al., 1999) and postmortem studies (Berg et al., 2002).

In our study, we both visually and quantitatively demonstrated a high overlap of QSM+ with TCS+ in PD patients. Visual inspection of the spatial distributions of QSM+ and PD-TCS+ (Fig. 2, bottom panel) shows a striking overlap along the axial extent of the midbrain. In particular, all QSM+ and PD-TCS+ regions are in very close vicinity to each other, i.e. in the SN and its surrounding structures, but nowhere else in the midbrain (see also Fig. 3). Quantitatively, we found a close to 46.0% overlap of the total QSM+ volume with PD-TCS+ in our cohort, and only a 4.3% overlap of QSM+ with HC-TCS+ (cf. Table 3), against the baseline of QSM+ overlap with the SN (36.4% overlap with SNc, and 6.0% overlap with SNr). From this, we conclude that TCS is more a marker of the increased, PD-related iron deposition in the SN than of the iron-based SN itself. The remaining 54% of non-overlap can be explained by several factors. The overlap regions in and around the SN are very small, and overlap measures are known to be sensitive to the size of the overlapping regions (Crum et al., 2006). Registration uncertainty, low voxel resolution, and the patchy nature of TCS+ speckle further contribute to this overlap sensitivity. Overall, it is quite

remarkable that QSM+ and TCS+ are in close vicinity, especially considering the absence of both within the rest of the midbrain area.

A noteworthy difference between TCS+ and QSM+ localization in PD, but also in HC, lies in the cranial part of the midbrain. Some areas of the brain have a higher level of iron than others like e.g. red nucleus, the anteromedial part of the subthalamic nucleus or the putamen (De Barros et al., Jul. 2019). An increased level of the brain iron in HC has been detected as a „normal“ aging process (Liu et al., 2016). It is still under discussion whether iron is a cause or consequence in neurodegeneration (Acosta-Cabronero et al., Jan. 2017). Our data leads us to the interpretation that TCS and QSM might not exactly represent the same iron pathology. They seem to represent different paths of iron accumulation (and other degenerated tissue) affecting nigro-striatal pathways, which might also be due to different iron states and bondings that the two modalities are able to detect. For example, TCS+ is being found in quiet early stages of PD and can predict a higher risk of getting PD in HC. It therefore may be able to detect a wider involvement of iron (and other components) than e.g. QSM, which detects only certain iron compositions. Further studies with follow-up examinations using both modalities would be needed to corroborate this notion.

A former PD-related study on QSM+ localization in the midbrain using voxel-based analysis (Du et al., 2016) shows locations which are visually consistent with ours. Authors also attribute a large part of QSM + to the SN, in particular its pars compacta sub-part. Similarly, QSM susceptibility analysis by Barbosa et al. (Barbosa et al., 2015) found QSM+ only in the area of SNc. Both studies identified significant QSM changes in PD dorso-medial to the SN, close to the red nucleus (Du et al., 2016). A further, recent study showed that in PD patients, the iron concentration increases in the ventral posterior SN over 3 years, as well as in the dorsal anterior region, while voxels outside the SN were not investigated (Bergsland et al., 2019). We detected similar differences in those regions based on voxel-wise analysis in the whole midbrain. As in previous studies, our main findings were located in the SNc, however, we also observed iron accumulation dorso-medial to that, in regions which we identified as the ventral tegmental area. The VTA is also named the A10 cell group and is divided into seven clusters (Fu et al., 2012): paranigral nucleus (PN), interfascicular nucleus (IF), caudal linear nucleus (CLi), and rostral linear nucleus (RLi), the parapeduncular nucleus (PaP), the parabrachial pigmented nucleus (PBP) and the rostral VTA (rVTA). There are several aspects connecting VTA to PD and potentially QSM+. The VTA in general consists mainly of dopaminergic neurons, especially in the PBP, next to GABAergic and glutamatergic neurons (Morales and Root, 2014; Olson and Nestler, 2007). Our main findings (both QSM+ and TCS+) within this area were located in the rVTA and the PBP. Furthermore, the VTA has mesocortical and mesolimbic pathways, and mesolimbic symptoms such as depression often develop in PD patients long before motor symptoms become obvious. It is noteworthy that VTA has been reported to have less severe dopaminergic cell loss in PD (Alberico et al., 2015; Damier et al., 1999; Maingay et al., 2006). Therefore, these regions in PD have not been focused on a lot in studies but have been reported to be affected by PD. They showed a clear degeneration in PD with a volume reduction of 42% in PBP and 31% in rVTA and assume a certain vulnerability in PD (McRitchie et al., 1997). The A10-subnuclei also show a high susceptibility to 6-OHDA which leads to a high rate of cell loss (Rodríguez et al., 2001). Aransay et al. (Aransay et al., 2015) found VTA neurons innervating cortical and/or basal forebrain structures, and neurons projecting toward the forebrain and brainstem. Especially the PBP shows a high innervation of either primary or secondary cortices.

Based on our results, and assuming that increased iron deposits in the VTA are a hallmark of neuronal destruction, we hypothesize that these processes might cause a dysfunction of the mesolimbic system which can be seen in quite early stages of PD.

4.3. Limitations

The analyzed sample in this study with 23 PD patients and 27 healthy controls is of limited size. An a-priori analysis regarding statistical power was not feasible due to the lack of comparable literature on multi-modal, quantitative analysis of TCS and MRI in the context of midbrain and PD. In a previous study (Plate et al., 2019), we used the same TCS image data as presented here, and analyzed it regarding the sensitivity and specificity of detection of PD, and the required sample size for analysis of TCS data was previously determined using an a-priori power analysis. We are convinced that the information presented here is of relevance, however future studies with larger sample sizes would be necessary to corroborate the results found here. A larger sample size might also allow for investigating iron distribution of PD patient groups separated by severity (as measured e.g. by UPDRS scores), which was not possible for the cohort size in this study.

In terms of TCS-MRI registration, only LC2 was tested, which was able to register 66.7% of TCS scans to MRI, but failed on 33.3%. Based on visual inspection, LC2 did not converge to a perceived optimum in failure cases. The main reasons seemed to be poor ICP initializations and poor visibility of registration-guiding structures inferior and superior to the midbrain area, due to narrow bone windows. Many of these failure cases were in fact very challenging even for a human observer, which ruled out manual fine-tuning of 3D registrations as a compensation. Future work could investigate alternative ultrasound-MRI approaches (Hu et al., 2012; Moradi et al., 2012; Kuklisova-Murgasova et al., 2013), but we believe that the bigger hurdle is general TCS image quality. Higher acoustic energy might improve tissue contrast, but maximum allowed energy transfer levels for diagnostic ultrasound cannot be exceeded. More promising approaches would be phase aberration correction approaches using real-time adaptive beamforming (Ivancevich et al., 2006) or patient-specific phase-interference compensators (Langton, 2018). Such approaches would not only help in improving image quality in 2D and 3D, but also geometric distortions, which we only considered along the y-axis of the TCS image plane and corrected for during TCS-MRI registration. However, these approaches assume specialized hard- and software which could not be considered for this work.

4.4. Conclusion

In this work, we acquired and analyzed a multi-modal atlas of the adult human brain incorporating TCS and QSM-MRI. Both modalities are capable of detecting iron accumulation, which accompanies the neurodegenerative process in Parkinson's disease. Our study concludes that PD-related increases in TCS and QSM signals demonstrate a high overlap along the entire axial extent of the midbrain. We confirm the established finding of iron accumulation in the substantia nigra pars compacta, and produce evidence that the ventral tegmental area and its sub-nuclei feature comparable alterations as well. Our results imply an earlier functional involvement of the mesolimbic system, rather than an isolated nigrostriatal loss of dopamine neurons.

Funding

This work was supported by the Lüneburg Heritage; the German Research Foundation (Deutsche Forschungsgesellschaft, DFG) [grant number BO 1895/4-1]; and the German Federal Ministry of Education and Health (BMBF) in connection with the foundation of the German Center for Vertigo and Balance Disorders (DSGZ) [grant number 01 EO 0901].

Supplementary material

None.

CRediT authorship contribution statement

Seyed-Ahmad Ahmadi: Conceptualization, Methodology, Software, Validation, Formal analysis, Investigation, Resources, Data curation, Writing - original draft, Visualization, Supervision, Project administration, Funding acquisition. **Kai Bötzel:** Conceptualization, Methodology, Investigation, Resources, Writing - review & editing, Supervision, Funding acquisition. **Johannes Levin:** Conceptualization, Methodology, Investigation, Writing - review & editing. **Juliana Maiostre:** Formal analysis, Data curation, Writing - review & editing, Project administration. **Tassilo Klein:** Methodology, Software, Validation, Investigation, Writing - review & editing. **Wolfgang Wein:** Methodology, Software, Validation, Investigation, Resources, Writing - review & editing. **Verena Rozanski:** Validation, Formal analysis, Writing - review & editing. **Olaf Dietrich:** Methodology, Software, Formal analysis, Writing - review & editing. **Birgit Ertl-Wagner:** Methodology, Software, Investigation, Resources, Writing - review & editing. **Nassir Navab:** Methodology, Software, Investigation, Resources, Writing - review & editing, Funding acquisition. **Annika Plate:** Conceptualization, Methodology, Software, Validation, Formal analysis, Investigation, Resources, Data curation, Writing - original draft, Visualization, Project administration, Funding acquisition.

Declaration of Competing Interest

None.

Acknowledgments

None.

References

Acosta-Cabronero, J., et al., Jan. 2017. The whole-brain pattern of magnetic susceptibility perturbations in Parkinson's disease. Brain 140 (1), 118–131.

Ahmadi, S.A., et al., 2011. Midbrain segmentation in transcranial 3D ultrasound for Parkinson diagnosis. Lect. Notes Comput. Sci. 6893 (LNCS, no. PART 3), 362–369.

Ahmadi, S.-A., Milletari, F., Nassir, N., Schuberth, M., Plate, A., Bötzel, K., Jun. 2015. 3D transcranial ultrasound as a novel intra-operative imaging technique for dbs surgery: a feasibility study. Int. J. Comput. Assist. Radiol. Surg. 10 (6), 891–900.

Alberico, S.L., Cassell, M.D., Narayanan, N.S., 2015. The vulnerable ventral tegmental area in Parkinson's disease. Basal Ganglia.

An, H., et al., Jan. 2018. Quantifying iron deposition within the substantia nigra of Parkinson's disease by quantitative susceptibility mapping. J. Neurol. Sci. 386, 46–52.

Aransay, A., Rodriguez-Lopez, C., Garcia-Amado, M., Clasca, F., Prensa, L., 2015. Long-range projection neurons of the mouse ventral tegmental area: a single-cell axon tracing analysis. Front. Neuroanat.

Avants, B.B., et al., 2010. The optimal template effect in hippocampus studies of diseased populations. Neuroimage 49 (3), 2457–2466.

Ayton, S., Lei, P., 2014. Nigral iron elevation is an invariable feature of Parkinson's disease and is a sufficient cause of neurodegeneration. Biomed. Res. Int.

Barbosa, J.H.O., et al., 2015. Quantifying brain iron deposition in patients with Parkinson's disease using quantitative susceptibility mapping, R2 and R2*. Magn. Reson. Imaging 33 (5), 559–565.

Becker, G., Seufert, J., Bogdahn, U., Reichmann, H., Reiners, K., 1995. Degeneration of substantia nigra in chronic Parkinson's disease visualized by transcranial color-coded real-time sonography. Neurology 45 (1), 182–184.

Berardelli, a, et al., 2013. EFNS/MDS-ES/ENS [corrected] recommendations for the diagnosis of Parkinson's disease. Eur. J. Neurol. 20 (1), 16–34.

Berg, D., et al., 1999. Iron accumulation in the substantia nigra in rats visualized by ultrasound. Ultrasound Med. Biol.

Berg, D., et al., 2002. Echogenicity of the substantia nigra: association with increased iron content and marker for susceptibility to nigrostriatal injury. Arch. Neurol. 59 (6), 999–1005.

D. Berg, "Marker for a preclinical diagnosis of Parkinson' s disease as a basis for neuroprotection," pp. 123–132, 2006.

Berg, D., et al., 2013. Enlarged hyperechogenic substantia nigra as a risk marker for Parkinson's disease. Move. Disord. 28 (2), 216–219.

Berg, D., et al., Jul. 2011. Enlarged substantia nigra hyperechogenicity and risk for Parkinson disease: a 37-month 3-center study of 1847 older persons. Arch. Neurol. 68, 932–937.

Bergsland, N., Zivadinov, R., Schweser, F., Hagemeier, J., Lichter, D., Guttuso, T., Jun. 2019. Ventral posterior substantia nigra iron increases over 3 years in Parkinson's disease. Mov. Disord. mds.27730.

Bernstein, M.A., Grgic, M., Brosnan, T.J., Pelc, N.J., 1994. Reconstructions of phase contrast, phased array multicoil data. Magn. Reson. Med. 32 (3), 330–334.

Brunser, A.M., et al., 2012. Transcranial doppler in a hispanic-mestizo population with neurological diseases: a study of sonographic window and its determinants. Brain Behav. 2 (3), 231–236.

Büttner-Ennever, J.A., Horn, A.K.E., 2014. Olszewski and Baxter's Cytoarchitecture of the Human Brainstem. Karger.

Crum, W.R., Camara, O., Hill, D.L.G., Nov. 2006. Generalized overlap measures for evaluation and validation in medical image analysis. IEEE Trans. Med. Imaging 25 (11), 1451–1461.

Damier, P., Hirsch, E.C., Agid, Y., Graybiel, A.M., 1999. The substantia nigra of the human brain: II. Patterns of loss of dopamine-containing neurons in parkinson's disease. Brain.

De Barros, A., Arribarat, G., Combis, J., Chaynes, P., Péran, P., Jul. 2019. Matching ex vivo MRI with iron histology: pearls and pitfalls. Front. Neuroanat. 13, 68.

Dexter, D.T., et al., 1987. Increased nigral iron content in postmortem Parkinsonian brain. The Lancet.

Dexter, D.T., et al., 1991. Alterations in the levels of iron, ferritin and other trace metals in parkinson's disease and other neurodegenerative diseases affecting the basal ganglia. Brain 114 (4), 1953–1975.

Du, G., et al., 2016. Quantitative susceptibility mapping of the midbrain in Parkinson's disease. Movement Disorders 31 (3), 317–324.

Fu, Y.H., Yuan, Y., Halliday, G., Rusznák, Z., Watson, C., Paxinos, G., 2012. A cytoarchitectonic and chemoarchitectonic analysis of the dopamine cell groups in the substantia nigra, ventral tegmental area, and retrorubral field in the mouse. Brain Struct. Funct.

Fuerst, B., Wein, W., Müller, M., Navab, N., 2014. Automatic ultrasound-MRI registration for neurosurgery using the 2D and 3D LC2 Metric. Med. Image Anal. 18 (8), 1312–1319.

Gerlach, M., Ben-Shachar, D., Riederer, P., Youdim, M.B.H., 1994. Altered brain metabolism of iron as a cause of neurodegenerative diseases? J. Neurochem. 63 (3), 793–807.

Hu, Y., et al., 2012. MR to ultrasound registration for image-guided prostate interventions. Med. Image Anal.

Hughes, A.J., Daniel, S.E., Kilford, L., Lees, A.J., 1992. Accuracy of clinical diagnosis of idiopathic Parkinson's disease: a clinico-pathological study of 100 cases. J. Neurol. Neurosurg. Psychiatr. 55 (3), 181–184.

Ivancevich, N.M., Dahl, J.J., Trahey, G.E., Smith, S.W., 2006. Phase-Aberration correction with a 3-D ultrasound scanner : feasibility study. Methods 53 (8), 1432–1439.

Jannin, P., Fitzpatrick, J.M., Hawkes, D.J., Pennec, X., Shahidi, R., Vannier, M.W., 2002. Validation of medical image processing in image-guided therapy. IEEE Trans Med Imaging.

Jenkinson, M., Beckmann, C.F., Behrens, T.E.J., Woolrich, M.W., Smith, S.M., 2012. FSL. Neuroimage 62 (2), 782–790.

Jesus-Ribeiro, J., Sargento-Freitas, J., Sousa, M., Silva, F., Freire, A., Januário, C., 2016. Substantia nigra hyperechogenicity does not correlate with motor features in Parkinson's disease. J. Neurol. Sci. 364, 9–11.

Kikinis, R., Pieper, S.D., Vosburgh, K.G., 2014. 3D Slicer: a platform for subject-specific image analysis, visualization, and clinical support. Intraoperative Imaging Image-Guided Ther. 277–289.

Klein, A., et al., 2009. Evaluation of 14 nonlinear deformation algorithms applied to human brain MRI registration. Neuroimage 46 (3), 786–802.

Kroll, C., Ahmadi, S.-A., Navab, N., Milletari, F., 2016. Coupling convolutional neural networks and hough voting for robust segmentation of ultrasound volumes. In: Proc. 38th German Conference on Pattern Recognition (GCPR),, to appear.

Kuklisova-Murgasova, M., et al., 2013. Registration of 3D fetal neurosonography and MRI. Med. Image. Anal.

Langkammer, C., et al., 2012. Quantitative susceptibility mapping (QSM) as a means to measure brain iron? A post mortem validation study. Neuroimage 62 (3), 1593–1599.

Langkammer, C., et al., 2015. Fast quantitative susceptibility mapping using 3D EPI and total generalized variation. Neuroimage 111, 622–630.

Langton, C.M., 2018. Passive twin-layer spatial-temporal phase-interference compensator for improved ultrasound propagation: a computer-simulation and experimental study in acrylic step-wedge samples. Appl. Acoustics.

Levin, J., et al., 2011. Generation of ferric iron links oxidative stress to α-synuclein oligomer formation. J. Parkinson's Dis. 1 (2), 205–216.

Li, D.-.H., He, Y.-.C., Liu, J., Chen, S.-.D., 2016. Diagnostic accuracy of transcranial sonography of the substantia nigra in Parkinson's disease: a systematic review and meta-analysis. Sci. Rep. 6 (1), 20863.

Liu, M., et al., 2016. Assessing global and regional iron content in deep gray matter as a function of age using susceptibility mapping. J. Magn. Resonance Imaging 44 (1), 59–71.

Lobsien, E., Schreiner, S., Plotkin, M., Kupsch, A., Schreiber, S.J., Doepp, F., 2012. No correlation of substantia nigra echogenicity and nigrostriatal degradation in Parkinson's disease. Mov. Disord. 27 (3), 450–453.

Lotfipour, A.K., et al., 2012. High resolution magnetic susceptibility mapping of the substantia nigra in Parkinson's disease. J. Magn. Resonance Imaging.

Maingay, M., Romero-Ramos, M., Carta, M., Kirik, D., 2006. Ventral tegmental area dopamine neurons are resistant to human mutant alpha-synuclein overexpression. Neurobiol. Dis.

McRitchie, D.A., Cartwright, H.R., Halliday, G.M., 1997. Specific A10 dopaminergic nuclei in the midbrain degenerate in Parkinson's disease. Exp. Neurol.

Menze, B.H., et al., 2015. The multimodal brain tumor image segmentation benchmark (BRATS). IEEE Trans. Med. Imaging 34 (10), 1993–2024.

Michaeli, S., et al., 2007. Assessment of brain iron and neuronal integrity in patients with Parkinson's disease using novel MRI contrasts. Movement Disorders 22 (3), 334–340.

Milletari, F., et al., 2017. Hough-CNN: deep learning for segmentation of deep brain regions in MRI and ultrasound. Comput. Vis. Image Understand. 164, 92–102.
Moradi, M., et al., 2012. Two solutions for registration of ultrasound to MRI for image-guided prostate interventions. In: Proceedings of the Annual International Conference of the IEEE Engineering in Medicine and Biology Society, EMBS.
Morales, M., Root, D.H., 2014. Glutamate neurons within the midbrain dopamine regions. Neuroscience.
Murakami, Y., et al., 2015. Usefulness of quantitative susceptibility mapping for the diagnosis of Parkinson disease. Am. J.Neuroradiol. 36 (6), 1102–1108.
Murphy, K., et al., 2011. Evaluation of registration methods on thoracic CT: the EMPIRE10 challenge. IEEE Trans. Med. Imaging 30 (11), 1901–1920.
Murty, V.P., Shermohammed, M., Smith, D.V., Carter, R.M., Huettel, S.A., Adcock, R.A., 2014. Resting state networks distinguish human ventral tegmental area from substantia nigra. Neuroimage 100, 580–589.
Olson, V.G., Nestler, E.J., 2007. Topographical organization of GABAergic neurons within the ventral tegmental area of the rat. Synapse.
Pauly, O., Ahmadi, S.-.A., Plate, A., Boetzel, K., Navab, N., 2012. Detection of substantia nigra echogenicities in 3D transcranial ultrasound for early diagnosis of parkinson disease. In: Medical image computing and computer-assisted intervention : MICCAI ... International Conference on Medical Image Computing and Computer-Assisted Intervention. 15. pp. 443–450.
Plate, A., Ahmadi, S.A., Pauly, O., Klein, T., Navab, N., Bötzel, K., 2012. Three-Dimensional sonographic examination of the midbrain for computer-aided diagnosis of movement disorders. Ultrasound Med. Biol. 38 (12), 2041–2050.
Plate, A., Maiostre, J., Levin, J., Bötzel, K., Ahmadi, S.-.A., 2019. A baseline study for detection of Parkinson's disease with 3D-transcranial sonography and uni-lateral reconstruction. J. Neurol. Sci. 397.
Rodríguez, M., Barroso-Chinea, P., Abdala, P., Obeso, J., González-Hernández, T., 2001. Dopamine cell degeneration induced by intraventricular administration of 6-hydroxydopamine in the rat: similarities with cell loss in Parkinson's disease. Exp. Neurol.
Schaefer, A., et al., 2016. Impact of consensus contours from multiple pet segmentation methods on the accuracy of functional volume delineation. Eur. J. Nucl. Med. Mol. Imaging 43 (5), 911–924.
Schweser, F., Deistung, A., Lehr, B.W., Reichenbach, J.R., 2011. Quantitative imaging of intrinsic magnetic tissue properties using MRI signal phase: an approach to in vivo brain iron metabolism? Neuroimage.
Shafieesabet, A., et al., Sep. 2017. Hyperechogenicity of substantia nigra for differential diagnosis of Parkinson's disease: a meta-analysis. Parkinsonism Relat. Disord. 42, 1–11.
Smith, S.M., 2002. Fast robust automated brain extraction. Hum Brain Mapp 17 (3), 143–155.
Sofic, E., et al., 1988. Increased iron (III) and total iron content in post mortem substantia nigra of parkinsonian brain. J. Neural Transm. 74 (3), 199–205.
S. Van De Loo et al., “Reproducibility and diagnostic accuracy of substantia nigra sonography for the diagnosis of Parkinson ’ s disease,” pp. 1087–1093, 2010.
Walter, U., et al., 2007. Transcranial brain sonography findings in discriminating between parkinsonism and idiopathic Parkinson disease. Arch. Neurol. 64 (11), 1635.
Walter, U., et al., 2016. Magnetic resonance-transcranial ultrasound fusion imaging: a novel tool for brain electrode location. Mov. Disord. 31 (3), 302–309.
Walter, U., Kanowski, M., Kaufmann, J., Grossmann, A., Benecke, R., Niehaus, L., Apr. 2008. Contemporary ultrasound systems allow high-resolution transcranial imaging of small echogenic deep intracranial structures similarly as MRI: a phantom study. Neuroimage 40 (2), 551–558.
Wein, W., 2018. Brain-Shift correction with image-based registration and landmark accuracy evaluation. Simulation, Image Processing, and Ultrasound Systems for Assisted Diagnosis and Navigation 146–151.
Wein, W., Ladikos, A., Fuerst, B., Shah, A., Sharma, K., Navab, N., 2013. Global registration of ultrasound to MRI using the LC2metric for enabling neurosurgical guidance. Lect. Notes Comput. Sci.
Wein, W., Pache, F., Röper, B., Navab, N., 2006. Backward-warping ultrasound reconstruction for improving diagnostic value and registration. In: Medical image computing and computer-assisted intervention : MICCAI ... International Conference on Medical Image Computing and Computer-Assisted Intervention. 9. pp. 750–757.
Xu, Y., et al., 2017. Large scale tissue histopathology image classification, segmentation, and visualization via deep convolutional activation features. BMC Bioinformatics 18 (1).
Youdim, M.B., Ben-Shachar, D., Eshel, G., Finberg, J.P., Riederer, P., 1993. {T}he neurotoxicity of iron and nitric oxide. {R}elevance to the etiology of {P}arkinson's disease. Adv. Neurol. 60, 259–266.
Yushkevich, P.A., et al., 2006. User-guided 3D active contour segmentation of anatomical structures: significantly improved efficiency and reliability. Neuroimage 31 (3), 1116–1128.